Improving the intrinsic conductance of selective area grown in-plane InAs nanowires with a GaSb shell

Wijden Khelifi, Christophe Coinon, M Berthe, David Troadec, G. Patriarche, X. Wallart, B Grandidier, L Desplanque

Improving the intrinsic conductance of selective area grown in-plane InAs nanowires with a GaSb shell

W. Khelifi[1], C. Coinon[1], M. Berthe[1], D. Troadec[1], G. Patriarche[2], X. Wallart[1], B. Grandidier[1] and L. Desplanque[,1]*

[1] Univ. Lille, CNRS, Centrale Lille, Univ. Polytechnique Hauts-de-France, Junia-ISEN, UMR 8520 - IEMN, F-59000 Lille, France

[2] Université Paris-Saclay, CNRS, Centre de Nanosciences et de Nanotechnologies, F-91120, Palaiseau, France

The nanoscale intrinsic electrical properties of in-plane InAs nanowires grown by selective area epitaxy are investigated using a process-free method involving a multi-probe scanning tunneling microscope. The resistance of oxide-free InAs nanowires grown on an InP(111)$_B$ substrate and the resistance of InAs/GaSb core-shell nanowires grown on an InP(001) substrate are measured using a collinear four-point probe arrangement in ultrahigh vacuum. They are compared with the resistance of two-dimensional electron gas reference samples measured using the same method and with the Van der Pauw geometry for validation. A significant improvement of the conductance is achieved when the InAs nanowires are fully embedded in GaSb, exhibiting an intrinsic sheet conductance close to the one of the quantum well counterpart.

I. INTRODUCTION

With its low electron effective mass and its strong spin orbit interaction, InAs exhibits exceptional electron transport properties that are particularly appealing for the fabrication of quantum devices involving Majorana bound states in hybrid semiconductor/superconductor one dimensional (1D) nanostructures [1-3]. One of the main technological challenges in this quest lies in the required material and interface quality to preserve the quantum coherence of electrons over a micrometre scale distance after standard semiconductor processing techniques.

Up to date, the best configuration to optimize the electron mean free path is generally obtained with a semiconducting layer sandwiched between larger band gap barriers that confine the charges into the channel and limit their interaction with surface or mismatch interface states, forming a two-dimensional electron gas (2DEG). For InAs channels, Al(Ga)Sb barriers offer a large conduction band offset enabling the formation of 2DEG with a Hall mobility as large as 1.85×10^6 cm^2.V^{-1}.s^{-1} at 1.3K on lattice matched GaSb substrate [4]. The hybridization gap that can be engineered in composite InAs/GaSb channel may also result in topologically protected edge states that could significantly improve the robustness of charge transport against disorder [5, 6]. However, processing 1D nanostructures from 2D quantum well results irremediably in a degradation of the transport properties caused by the sidewall surface states after etching. Bottom-up approaches involving the Vapor Liquid Solid (VLS) growth of vertical InAs nanowires (NWs) and their subsequent transfer on a host substrate for processing have emerged to avoid nanoscale semiconductor etching [7-10]. Controlling the position of the nucleation and organizing the growth of vertical NWs into arrays have been enabled by combining the design of nanoholes in a dielectric mask on the substrate with the selective area epitaxy (SAE) of NWs [11-14]. Later, this technique have evolved toward template assisted epitaxy [15] and in-plane SAE in order to achieve more complex architectures and a scalable nano-device process [16].

When grown in this latter configuration, the good control of the NW conductivity requires the use of semi-insulating substrates. However, the large lattice mismatch of InAs with standard III-V semi-insulating substrates such as GaAs or InP prevents the formation of high quality InAs NWs with competitive electron mobility. A compromise consists in growing a thick metamorphic buffer layer to limit the impact of surface roughness and threading defects on transport properties when the growth occurs at full wafer scale [17, 18]. This drawback can also be limited by nanoscale selective area epitaxy on (111) oriented substrates [19, 20] or by using a thin nanoscale template to reduce the mismatch prior to InAs deposition on GaAs(001) substrates [21-23].

In this paper, we investigate the intrinsic conductance of InAs NWs grown by SAE. To minimize the number of processing steps to contact the NWs, the electrical conductance is measured with four-probe Scanning Tunneling Microscopy (4P-STM), which allows the arbitrary arrangement of non-invasive probe electrodes onto a single NW [24]. Two sets of NWs are considered and benchmarked with InAs-based 2DEG grown on GaAs(001) substrates. The first type of NWs corresponds to InAs NWs directly grown on InP(111)$_B$, as such a substrate favors the growth of nearly defect-free InAs NWs [25]. In this case, the removal of a thin amorphous arsenic protecting layer prior to the transport measurements in Ultra-High Vacuum (UHV) ensures the formation of ohmic contacts on oxide-free facets. The second type of NWs deals with InAs/GaSb core-shell NWs grown on InP(001). For both types of NWs, the knowledge of the geometry of 100 nm and 200 nm-wide InAs channels based on electron microscopies allows to determine their sheet

resistances. These experiments reveal the benefit of embedding the InAs NWs in GaSb, which shows a sheet resistance close to the analog 2D heterostructure.

II. EXPERIMENTAL DETAILS

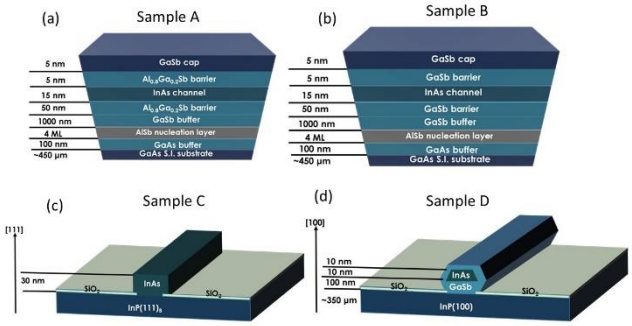

FIG. 1. Schematic structure of the grown samples: (a) InAs/AlGaSb quantum well grown on GaAs (001), (b) InAs/GaSb quantum well grown on GaAs (001), (c) in-plane InAs NWs grown on InP(111)$_B$ and (d) InAs/GaSb core-shell nanostructures grown on InP(001).

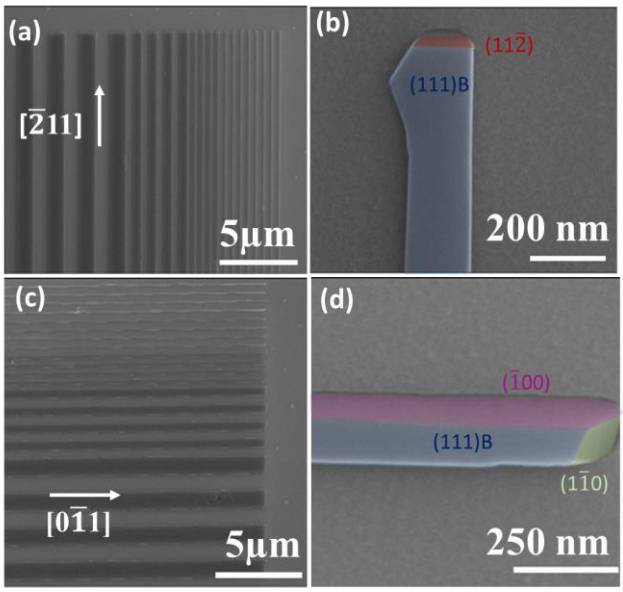

FIG. 2. SEM images of InAs NW arrays grown by SAE on InP(111)$_B$ (sample C). Each array is composed of a series of four 20 µm-long NWs inside mask apertures with widths of 500 nm, 200 nm, 100 nm or 50 nm. The NWs are oriented along the (a) [$\bar{2}$11] and (c) [0$\bar{1}$1] crystallographic directions. (b) and (d) SEM images of NW end patterned along the [$\bar{2}$11] and [0$\bar{1}$1] crystallographic directions with a mask aperture width of 100 nm wide. The different facets of the NWs are highlighted with false colors (red for the (11$\bar{2}$) facet, blue for the (111) facets, purple for the ($\bar{1}$00) facet and green for the (1$\bar{1}$0) facet).

The different samples used in this experiment are grown by Molecular Beam Epitaxy (MBE) in a RIBER Compact 21 system equipped with valved cracker cells for As and Sb evaporation. A RF plasma cell is also set-up on the system to produce an atomic hydrogen flux used for substrate deoxidization and selectivity improvement during SAE of GaSb [23]. The different III element fluxes are calibrated by recording the Reflection High Energy Electron Diffraction (RHEED) specular intensity oscillations during the homoepitaxy of InAs or GaAs for indium and gallium respectively or during the growth of AlAs on GaAs for aluminium. As and Sb fluxes are calibrated using V-element limited RHEED specular intensity oscillations during the homoepitaxy of GaAs and GaSb respectively.

The first set of samples (A and B) consists of two InAs channel based heterostructures grown on GaAs(001) semi-insulating substrates as described in figure 1a and 1b. In both structures, the large mismatch between InAs and GaAs is accommodated thanks to a buffer layer composed of a 4 monolayer (ML) AlSb nucleation layer and a 1 µm-thick GaSb layer [26]. In sample A, the 15 nm-thick InAs channel is sandwiched between $Al_{0.8}Ga_{0.2}Sb$ barriers with a thickness of 50 nm for the bottom one and 5 nm for the top one. In sample B, the InAs channel is sandwiched between GaSb barriers with the same thickness. In both cases, a 5 nm-thick GaSb cap is deposited on top of the epitaxial structure to prevent the oxidation of AlGaSb for sample A and keep the same surface to channel distance for sample B. As shown in the simulation of the charge carrier density in the structure (figure S1, supplementary information), sample A should exhibit a type II band-line up between the InAs channel and the $Al_{0.8}Ga_{0.2}Sb$ barrier whereas a broken gap band-line up between InAs and GaSb barriers should be obtained for sample B. This leads to the presence of an additional 2D hole gas concentrated in the GaSb bottom barrier at the interface with the overlying InAs channel whereas only a single 2DEG located in the InAs channel is obtained in the case of AlGaSb barriers.

The second set of samples (C and D) consists of selective area grown in-plane InAs NWs on semi-insulating InP substrates. Prior to the epitaxial growth, a 30 nm-thick SiO_2 mask is prepared by means of plasma enhanced chemical vapour deposition, e-beam lithography, reactive ion etching and a final dilute HF treatment enabling the design of apertures as narrow as 50 nm in the SiO_2 mask [27]. The geometry of most of the apertures corresponds to a segment with different in-plane orientations. A limited number of more complex geometries such as crosses is also considered. After the final HF treatment, the width corresponding to 100nm and 200nm nominal apertures are respectively about 130 and 230 nm. After outgassing the substrate for one hour at 200°C in a preparation chamber, the InP native oxide covering the bottom surface of the apertures is removed. This deoxidation process is performed by annealing the substrate under As_4 flux and exposing it to atomic hydrogen for 30s while rising up the substrate temperature to 500°C. Sample C consists of a semi-insulating InP(111)$_B$ substrate, where InAs NWs are directly grown at 390°C inside the oxide-free apertures at a growth rate of 0.05ML.s^{-1} and a very large As_4/In flux ratio of 110. The nominal thickness of the deposition is 30 nm. After growth, the SiO_2 layer in between the NWs is chemically removed with an HF treatment. Then, the sample is re-introduced in the MBE system and the surface is deoxidized with an annealing up to 400°C under As_4 and atomic hydrogen exposure. The substrate is then cooled down to 10°C and capped with amorphous arsenic for several minutes in order to prevent the surface from oxidation during the transfer to the 4P-STM.

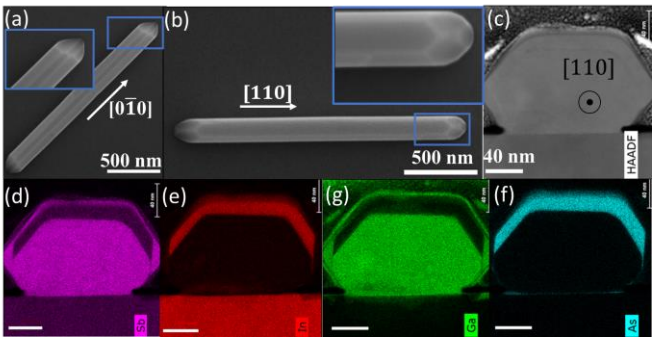

FIG. 3. SEM micrographs of in-plane InAs/GaSb NWs grown by SAE on InP(001) (sample D). The 100 nm-wide NWs are oriented along (a) the [0$\bar{1}$0] and (b) [110] crystallographic directions. Insets: Magnified view of the NW end. (c) Cross-sectional high angle annular dark field (HAADF) STEM image of an InAs/GaSb NW oriented along the [110] crystallographic direction. Elemental mapping of the NW for (d) Sb, (e) In, (g) Ga and (f) As.

For sample D, the mask is designed on a semi-insulating InP(001) substrate and consists of apertures with length of several micrometres and widths of 100 nm or 200 nm. The apertures are oriented along the [110] or [**0$\bar{1}$0**] directions. After the removal of the InP oxide as described above for sample C, a 100 nm-thick GaSb layer is first grown at a temperature of 470°C, with a growth rate of 0.1ML.s^{-1}, a Sb/Ga flux ratio of 2.5 and under atomic hydrogen exposure. These conditions have been demonstrated suitable for selective epitaxy as well as to optimize the GaSb nanostructure morphology on GaAs or InP (001) substrates [21, 28]. InAs is then deposited on the GaSb nano-template with a nominal deposited thickness of 10 nm. A 10 nm-thick GaSb cap is finally deposited on the nanostructures.

The morphology of the nanostructures is analysed using Scanning Electron Microscopy (SEM), Atomic Force Microscopy (AFM) and, for some NWs, Scanning Transmission Electron Microscopy (STEM) after preparation of thin cross-sections through the in-plane NWs using Focus Ion Beam (FIB) etching. The STEM studies are performed in a Titan Themis 200 (FEI) microscope equipped with a spherical aberration corrector on the probe and an Energy-Dispersive X-ray spectroscopy (EDX) system super X (0.7 srad solid angle of collection). The accelerating voltage is 200 kV. The (half) convergence angle of the probe is 17.6 mrad and the probe current 85 pA.

The transport properties of 2DEG in samples A and B are investigated at 300 K and 77 K by Hall measurements after the fabrication of Van der Pauw devices using optical lithography, chemical etching of the epitaxial layer down to the GaAs substrate and indium contact deposition. A picture of sample A after the Van der Pauw device fabrication can be seen in the right inset of figure 6. In parallel, the sheet resistance of the 2DEG in samples A and B is also deduced from the 4-probe measurements of the resistance with 4P-STM working in UHV (Nanoprobe, Omicron Nanotechnology). As the use of good electrical contacts is essential to inject and extract charge carriers, tungsten tips are prepared by an electrochemical etching in NaOH and thoroughly annealed in the UHV preparation chamber to remove the thin oxide layer covering the tips.

Prior to the 4P-STM transport measurements, all the samples are annealed at 120°C in UHV for a few hours. The InAs NWs grown on the InP(111)$_B$ substrate are further annealed at 320 °C to remove the As capping layer, while monitoring the As desorption with mass spectroscopy. For all the samples, the STM tips are always positioned with an in-line four-point geometry under the control of a SEM. The STM tips are first brought into electrical contact with the surface of the samples using the distance regulation of the STM control system. Then, a stable electric contact is obtained by further pushing down the STM tips in the feedback-off mode. Injection of the current I through the outer tips and measurement of the voltage drop V between the two inner tips give access to the four-point resistance. For the quantum well, the 4-point resistance is measured for different equidistant separations between the STM tips at temperatures of 300 K and 115 K. In the case of the NWs, the two outer tips are connected at the end of the NWs. An inner tip is connected close to one outer tip and kept fixed. The fourth tip is moved step by step from one side of the NW to the other one to acquire $V(I)$ characteristics with different separations between the inner tips.

III. RESULTS AND DISCUSSION

Figure 2 displays the morphology of arrays of selective area grown in-plane InAs NWs with different widths and orientations that can be observed on sample C before mask removal and As cap layer deposition. It reveals a very good selectivity with respect to SiO_2 and a uniform filling of the mask apertures with clean and well defined facets whose nature is determined by the aperture direction with respect to the (111)$_B$-oriented substrate (figure S2). Whatever the aperture direction, the nanostructures are delimited by a top (111) surface. The atomic force microscope profile performed on an array of parallel NWs (figure S3) indicates that the top (111) surface is lying about 25 nm above the SiO_2 surface which is consistent with a nominal NW thickness deposition of 30 nm and a SiO_2 mask thickness of ~10 nm remaining after HF treatment prior to the growth.

On the InP(001) substrate, the growth of a GaSb nano-template prior to the InAs film is necessary to ensure the continuity of a thin channel in the mask apertures. The SEM observations performed on sample D confirm the excellent selectivity and the very good continuity of the in-plane nanostructures in [**0$\bar{1}$0**] and [110] directions with well-defined facets (figure 3 and figure S4). The cross-sectional STEM analysis performed on a [110]-oriented NW and the associated EDX analysis reveals that the InAs channel adopts the shape of the underlying GaSb template with two lateral tilted wings grown on the (111) facets of the GaSb hexagonal prism (figure 3c-f). This is also true when the width changes from 100 nm to 200 nm (figure S5a). On the top (001) plane of the GaSb template, the InAs channel thickness is about 15 nm, slightly larger than the intended thickness. The same analysis also shows that the InAs channel is fully covered with GaSb even at the edge of the wings, preserving it from further oxidation. In the [**0$\bar{1}$0**] direction, the GaSb template looks more like a flattened cylinder for both widths of 100 nm and 200 nm (figure S5d and g). The growth of the InAs channel occurs predominantly on the top (001) GaSb facet, with two small separated channels observed on the sidewall of the GaSb template. Once again, the HAADF-STEM images show that the light grey-colored top InAs channel is embedded in GaSb

and, hence, protected from further oxidation. The TEM bright field micrographs of figure S6 reveal that, despite the interface dislocation array formed at the GaSb/InP interface, some threading dislocations are still present inside the GaSb buffer. Their density appears to decrease with narrower apertures. For 100 nm wide ones, we note that the threading segments do not seem to reach the top InAs channel where neither threading dislocations nor stacking faults or twin defects are observed.

Both types of NWs are characterized with the 4P-STM set-up for the main crystallographic orientations of the nanowires, i.e, the [010] and [110] orientations for NWs grown on InP (001) substrates and the [$\mathbf{0\bar{1}1}$] and [$\mathbf{\bar{2}11}$] orientations for NWs grown on InP $(111)_B$ substrates. Whatever the chemical nature of the top facet in electrical contact with the STM tips, the variation of the potential measured with the inner probes as a function of the current injected and collected by the outer probes is linear. The slope of the $V(I)$ curves yields the four-point resistance, R_{4P}. As shown in figures 4 and 5 (also figures S7 and S8), R_{4P} varies linearly with the separation of the inner tips, consistent with a diffusive transport regime. The resistance per unit length is about a few $k\Omega.\mu m^{-1}$, with a smaller resistance for the NWs embedded in GaSb. Such a range is comparable with the values of R_{4P} measured for free-standing InAs NWs with a slightly larger diameter and grown based on the VLS mechanism [29]. It is also consistent with the resistance per unit length measured on InAs NWs grown on top of GaAs nanomembranes [21] and InAs NWs based on a template-assisted selective epitaxy when the diffusive transport regime is reached [15].

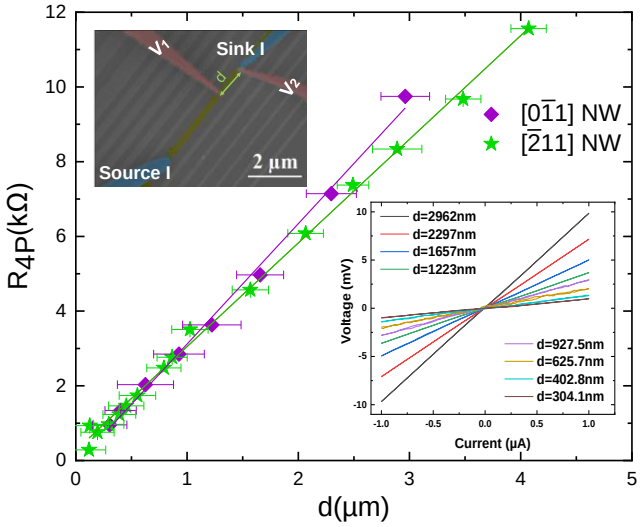

FIG. 4. Variation of the four-point probe resistance measured at different inner probe distances d on a bare [0$\bar{1}$1]-oriented InAs NW (purple diamond) and on a bare [$\bar{2}$11]-oriented InAs NW (green stars), both with an aperture width of 100 nm. Purple and green lines are best linear fits of the data, from which the resistance per unit of length is extracted. Top inset. SEM image of the [$\bar{2}$11]-oriented InAs NW grown on the $InP(111)_B$ substrate and in electrical contact with the four STM tips. The outer tips, which inject and collect the current are labelled Source I and Sink I, the inner tips, which measure the potential drop along the wire, are labelled V_1 and V_2. Bottom inset: $V(I)$ curves measured at different tip separations and corresponding to the set of purple diamond data.

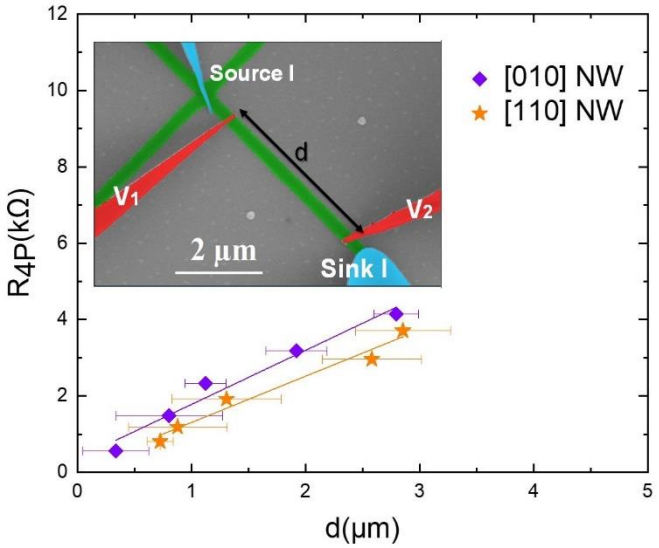

FIG. 5. Variation of the four-point probe resistance measured at different inner probe distances d on a [010]-oriented InAs/GaSb core-shell NW (purple diamond) and on the [110]-oriented segment of an InAs/GaSb core-shell cross (orange stars), both with an aperture width of 100 nm. Purple and orange lines are best linear fits of the data, from which the resistance per unit of length is extracted. Inset. SEM image of an InAs/GaSb core-shell cross grown on the InP(001) substrate. The [110]-oriented segment is in electrical contact with the four STM tips. The outer tips, which inject and collect the current are labelled Source I and Sink I, the inner tips, which measure the potential drop along the wire, are labelled V_1 and V_2.

To assess the electrical quality of the NWs, four-point probe measurements of the resistance are also performed with samples A and B. As shown in figure 6, the R_{4P} values are almost constant whatever the equidistant tip separation between 100 μm down to a few microns for both temperatures of 300 K and 115 K. Such a behavior is consistent with a 2D conductance [24]. As the four-point probe method shows some fluctuations, due to a small misalignment in the positioning of the STM tips, the transport properties of the 2D heterostructures are further studied with the Van der Pauw structures built in other areas of the same samples (right inset of Fig.6). The Hall data of samples A and B are summarized in table 1.

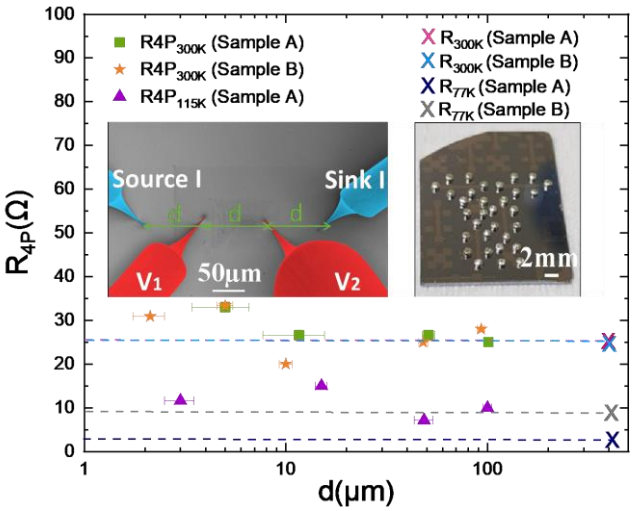

FIG. 6. Variation of the four-point probe resistance as a function of equidistant probes separations. The resistances deduced from the Van

der Pauw devices are also indicated (cross) and horizontal lines intersecting these resistances are used as guidelines for comparison. Inset (left): SEM image of four collinear STM tips in electrical contact with Sample A at 300 K. The outer tips, which inject and collect the current are labelled Source I and Sink I, the inner tips, which measure the potential drop along the wire, are labelled V_1 and V_2. Right inset: photograph of a Van der Pauw sample.

At 300 K, quasi-identical Hall resistances are achieved for both heterostructures, the higher mobility in sample A (33500 $cm^2.V^{-1}.s^{-1}$) being compensated by a lower sheet carrier density. At 77 K, the electron mobility increases to more than 300000 $cm^2.V^{-1}.s^{-1}$ for sample A with AlGaSb barriers whereas sample B exhibits half of this value. This difference is attributed to the lower conduction band offset between GaSb and InAs, which limits the electron confinement in the channel and expands a significant part of the electron wave function inside the larger electron effective mass GaSb barriers. Despite the type III configuration of the InAs/GaSb system and the thick GaSb buffer layer, it is interesting to notice that the transport is dominated by the electrons flowing in the InAs channel with a high mobility.

Temperature	Sample	Hall mobility ($cm^2.V^{-1}.s^{-1}$)	Hall density (cm^{-2})	Sheet resistance (Ω/□)
300 K	A	33 500	$1.60x10^{12}$	117
	B	26 000	$2.10x10^{12}$	115
77 K	A	301 000	$1.26x10^{12}$	16
	B	150 000	$1.00x10^{12}$	42

Table 1. Hall data measured on the 2DEG of samples A (AlGaSb/InAs heterostructure) and B (InAs/GaSb heterostructure).

For comparison of the resistance between both techniques, the sheet resistance found with the Van der Pauw geometry is converted into a four-probe resistance [24],

$$R_{4P} = \frac{ln2}{\pi} R_{sh} \quad (1)$$

The results are plotted in figure 6. Although the separation between the macroscopic electrodes is larger than the STM tip separations, the data fall into the range of the measured resistances with 4P-STM at room and low temperatures, demonstrating the high quality of the heterostructures across the samples.

The resistances per unit of length measured for all the NWs are normalized by their width, which is deduced from the cross-sectional STEM analysis. For that purpose, the total width of the InAs channel for the [110]-oriented InAs/GaSb core-shell NWs takes into account the top (001) facet and the (111) side facets. Although the channel thickness seems reduced on the (111) facets, we assume a constant thickness of the InAs channel for the calculation of the sheet resistance. This approximation slightly over-estimates the sheet resistance values for [110]-NWs. Conversely, only the width of the top channel is considered for the [010]-oriented InAs/GaSb core-shell NWs. As the charge density is propably highly non uniform within the thickness of the InAs channel, we do not compare the resistivity of the different channels but the sheet resistance. This is particularly true for the 30 nm-thick InAs NWs without GaSb cap where the charge density results from the surface Fermi level pinning in the conduction band. Figure 7 summarizes the sheet resistances estimated on the different NWs for both NW widths of 100 nm and 200 nm and compares them with the sheet resistance found in the Van der Pauw structures obtained at room temperature. When the InAs NWs are directly grown on the $(111)_B$-oriented InP substrate, whatever the orientation of the NWs is, the sheet resistance is about two times higher than the one for the InAs/GaSb core-shell NWs. This result is consistent with the observation of a doubling of the mobility when an InGaAs buffer layer is used in SAE NWs grown on GaAs (001) substrate to improve the interfacial quality of the InAs NWs [23]. It shows the key role of the pseudomorphic barriers that surround the InAs channel to reduce the deleterious effect of the surface states or mismatch interface states on the transport properties. For the [110]-oriented core-shell NWs, shrinking the width of the aperture seems to improve the sheet resistance. This is consistent with the reduction of the density of dislocations that originate from the mismatched GaSb/InP interface and thread up to the InAs channel as shown in figure S6.

Thanks to the presence of the GaSb buffer and capping layers, the conductance of the InAs channel is close to the one of the 2D InAs/GaSb heterostructure of samples A and B at 300 K. If one considers a sheet electron concentration in the InAs NWs of sample D similar to the one obtained from the Hall measurements in samples A and B (~$2x10^{12}$ cm^{-2}), this implies an electron mobility as large as 16600 $cm^2.V^{-1}.s^{-1}$ at room temperature for the 100 nm-wide [110]-oriented NWs.

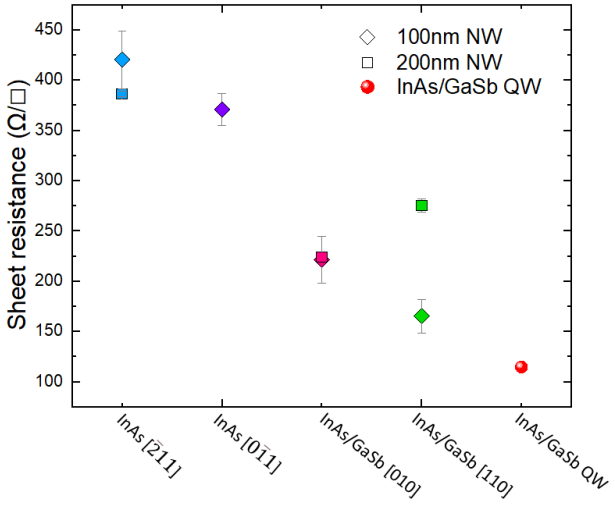

FIG. 7. Sheet resistance estimated from four-probe resistance measurements on NWs of sample C and D and benchmarked with the sheet resistance of InAs/GaSb 2DEG (sample B).

IV. CONCLUSION

The sheet conductance of in-plane InAs NWs grown on InP substrate and measured by 4P-STM is significantly improved when the InAs channel is embedded in a GaSb shell. The shell protects the electrons from surface state as well as mismatch accommodation scattering. While still larger than the conductance measured by Hall effect and confirmed by 4P-STM measurements on InAs/GaSb 2DEG, its value is close to the quantum well conductance at room temperature. Further investigations are now needed to evaluate the transport properties of InAs/GaSb in-plane NWs at cryogenic temperature. But the estimated mobility values at room

temperature are promising to achieve a mean free path of carriers sufficiently large at low temperature for coherent quantum device fabrication.

ACKNOWLEDGEMENTS

This study was financially supported by the French National Research agency (INSPIRING project ANR-21-CE09-0026-01), the IEMN PCMP-PCP and CMNF platforms of the French Technological Network RENATECH, and the Région Hauts de France.

REFERENCES

[1] A.Das et al, *Nature Phys* 8, 887–895 (2012)
[2] M.T.Deng et al, *Science* 354 (2016), 1557
[3] S.Vaitiekėnas et al, Nat. Phys. 17, 43–47 (2021)
[4] T. Tschirky et al, *Phys. Rev.* B 95, 115304 (2017)
[5] C.Liu et al, *Phys. Rev. Lett*. 100,236601 (2008)
[6] I.Knez et al, *Front. Phys.*, 2012, 7(2): 200–207
[7] S. M. Albrecht, *Nature* 531 (2016) 206
[8] M.Nillson et al, *Phys. Rev.* B94, 115313 (2016)
[9] T.Rieger et al, *Nanoscale* 7, 356 (2015)
[10] O.Arif et al, *Crystal Growth & Design* **2020** *20* (2), 1088-1096
[11] K.Tomioka et al, *Nano letters* 8, 3475 (2008)
[12] S.Hertenberger et al, *J. Appl. Phys.* 108, 114316 (2010)
[13] J. Seidl et al, *Nano Letters* **2019** *19* (7), 4666-4677
[14] G.Grégoire et al, Cryst. Growth Des. 2021, 21, 9, 5158–5163
[15] J.Gooth et al, *Appl. Phys. Lett*. 110, 083105 (2017)
[16] S. Vaitiekėnas et al, *Phys. Rev. Lett*. 121,147701 (2018)
[17] H.-R.Blank et al, *Appl. Phys. Lett.* 69, 2080 (1996)
[18] L.Desplanque et al, *Journal of Crystal Growth* 301–302 (2007) 194–198
[19] M.Friedl et al, *Nano Lett.* 2018, 18, 2666−2671
[20] J.-S.Lee et al, *Phys. Rev.* Mat. 3, 084606 (2019)
[21] M.Fahed et al, *Nanotechnology* 27 (2016) 505301
[22] M.Fahed et al, *Journal of Crystal Growth* 477 (2017) 45–49
[23] D.V. Beznasyuk et al, *Phys. Rev. Mat*. 6, 034602 (2022)
[24] I.Miccoli et al, *J. Phys. Condens. Matter.* 27, p. 223201 (2015)
[25] P.Aseev et al *Nano letters*, 19(1), 218-227
[26] Y. Wang et al, *J. Appl. Phys*., 2011, 109, pp.023509-1-6
[27] L.Desplanque et al, *Nanotechnology* 25 (2014) 465302
[28] A.Bucamp et al, *Nanotechnology* 33 (2022) 145201
[29] C.Durand et al, *Nanotechnology*, 24 (2013), 275706

Improving the intrinsic conductance of selective area grown in-plane InAs nanowires with a GaSb shell
(Supplementary information)

W. Khelifi[1], C. Coinon[1], M. Berthe[1], D. Troadec[1], G. Patriarche[2], X. Wallart[1], B. Grandidier[1] and L. Desplanque[,1]*

[1] Univ. Lille, CNRS, Centrale Lille, Univ. Polytechnique Hauts-de-France, Junia-ISEN, UMR 8520 - IEMN, F-59000 Lille, France

[2] Université Paris-Saclay, CNRS, Centre de Nanosciences et de Nanotechnologies, F-91120, Palaiseau, France

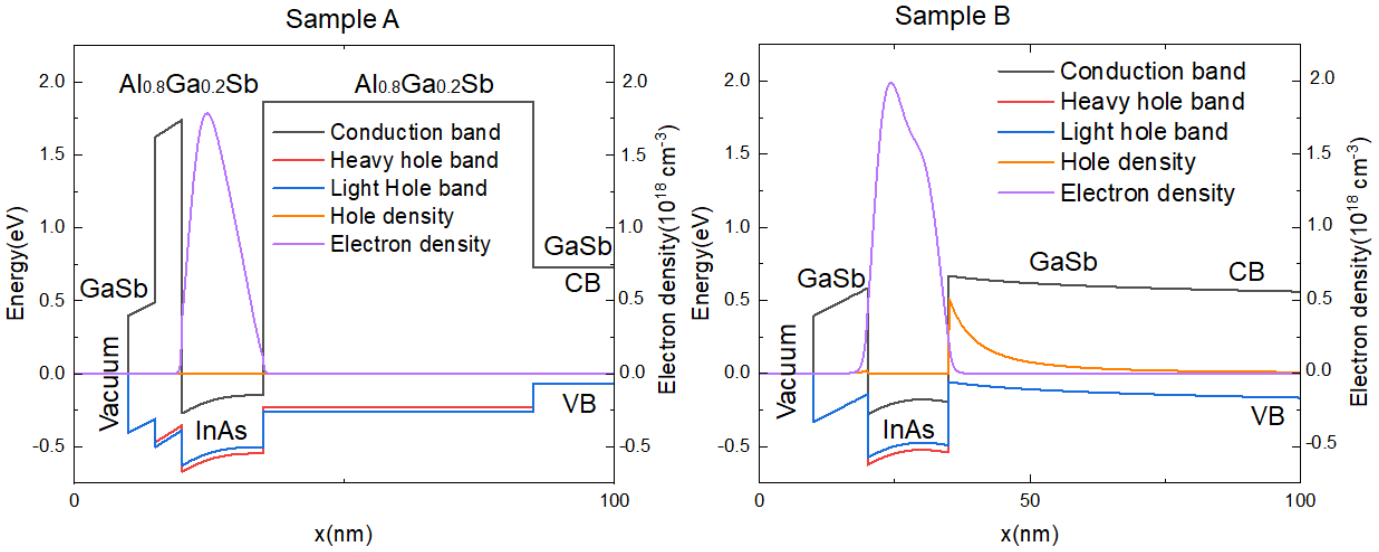

FIG. S1. Band diagram simulation of the 2DEG formed in sample A (left) and sample B (right) using Nextnano software [1]

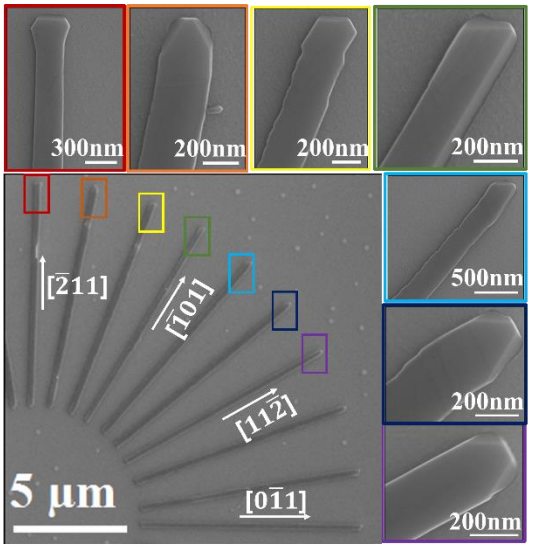

FIG. S2. SEM images of 200 nm-wide InAs NWs with different in-plane orientations (rotation every 10° from [$\mathbf{0\bar{1}1}$] to [$\mathbf{\bar{2}11}$]) grown by SAE on InP(111)$_B$ (sample C). The different facets that are formed at the end of the NWs are highlighted in the different insets.

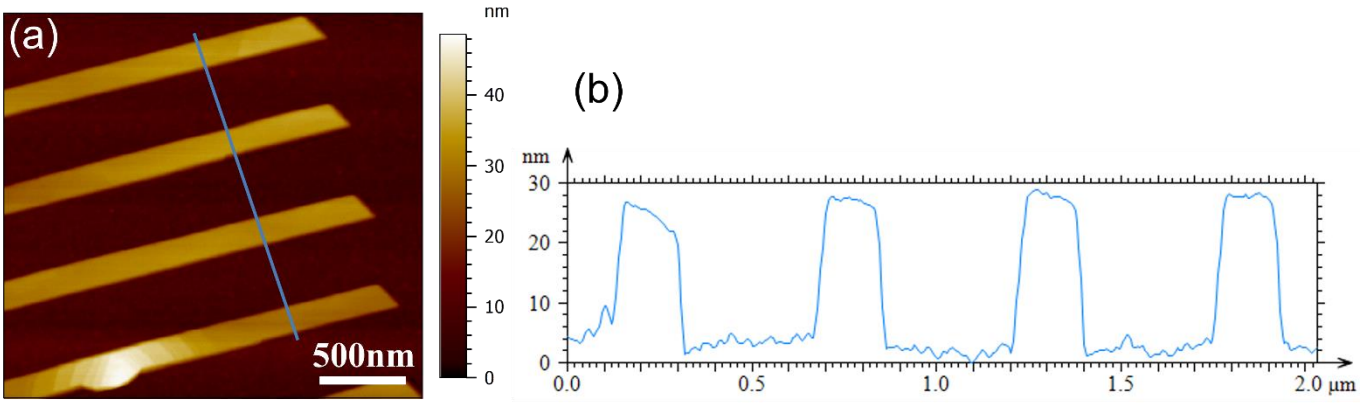

FIG. S3. (a) AFM image observed on an array of in-plane 100 nm-wide InAs NWs grown by SAE on InP(111)$_B$ (sample C). (b) Height profile along the blue line plotted in the AFM image.

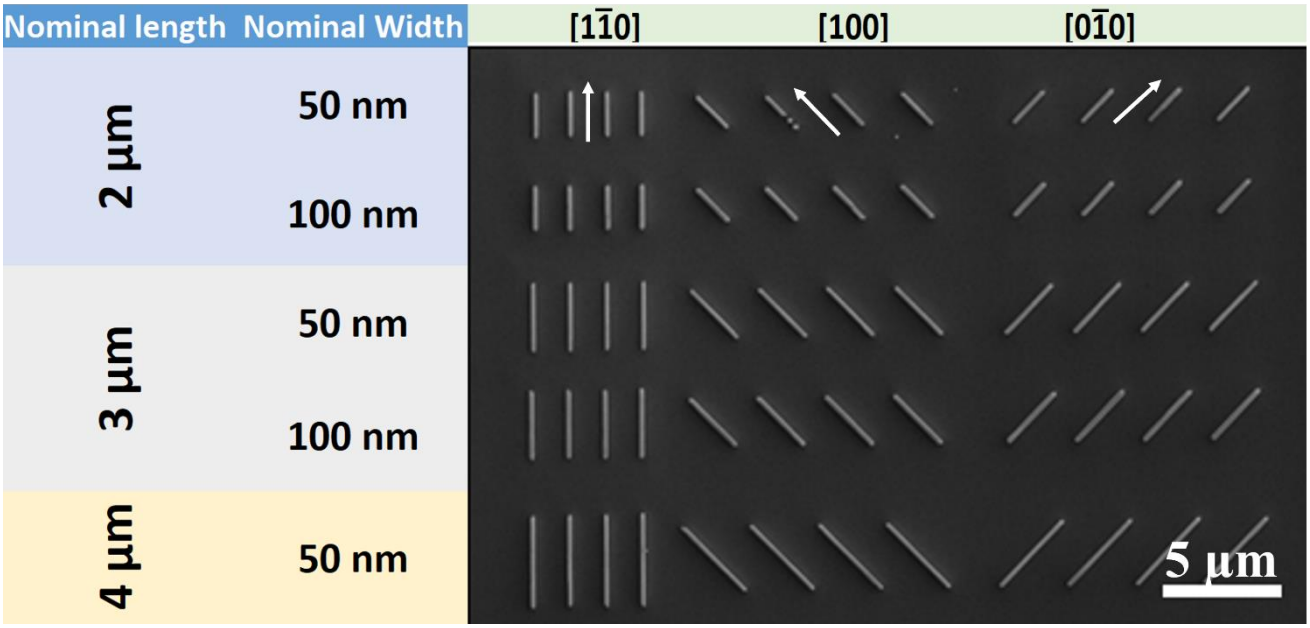

FIG. S4. SEM image of arrays of in-plane InAs/GaSb NWs grown by SAE on InP(001) (sample D). .

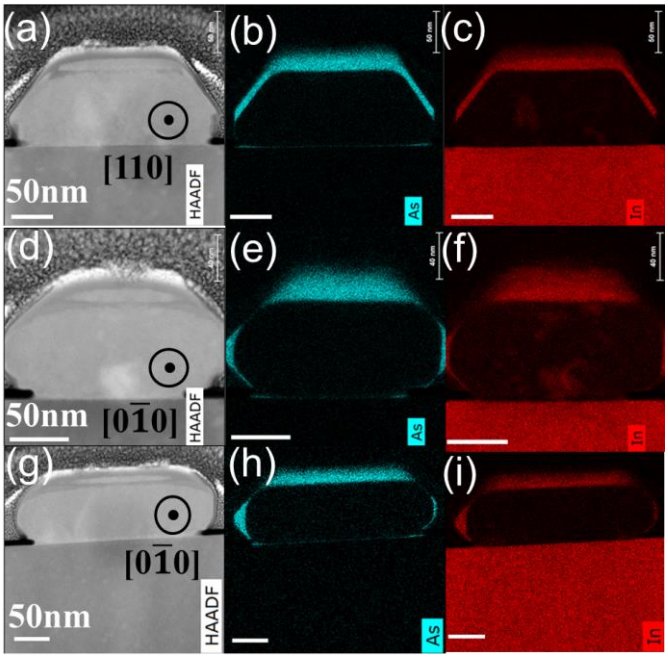

FIG. S5. Cross-sectional HAADF micrographs of in-plane InAs/GaSb NWs on InP(001) (sample D) inside (a) a 200 nm-wide mask aperture oriented along [110], (d) a 100 nm-wide mask aperture oriented along [0$\bar{1}$0] and (g) a 200 nm-wide mask aperture oriented along [0$\bar{1}$0]. (b,c; e,f; h,j) Related elemental mapping of As and In respectively. Scale bars correspond to 50 nm.

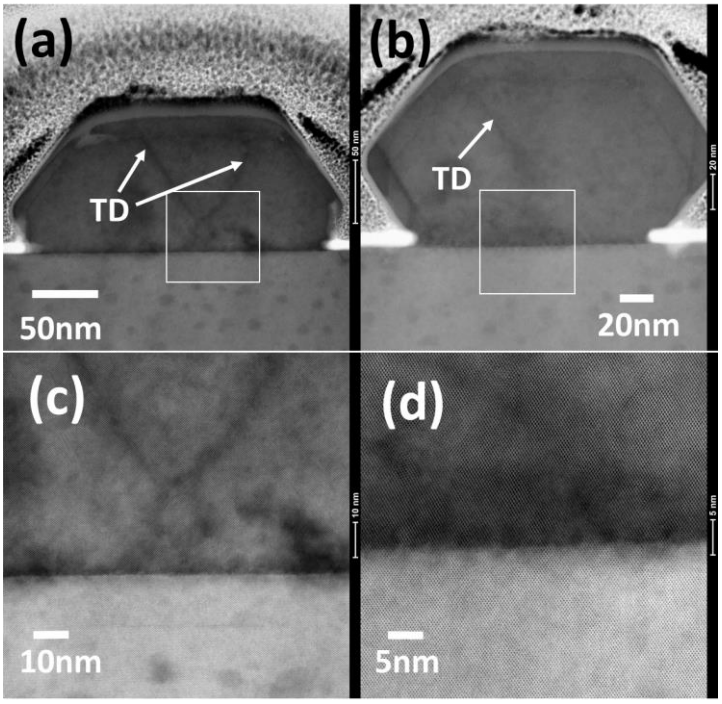

FIG. S6. TEM bright field micrographs of in-plane InAs/GaSb NWs (sample D) grown inside (a and c) a 200 nm-wide mask aperture or (b and d) a 100 nm-wide mask aperture. (c) and (d) are magnified views of the InP/GaSb interface inside the white rectangles indicated in images (a) and (b) respectively.

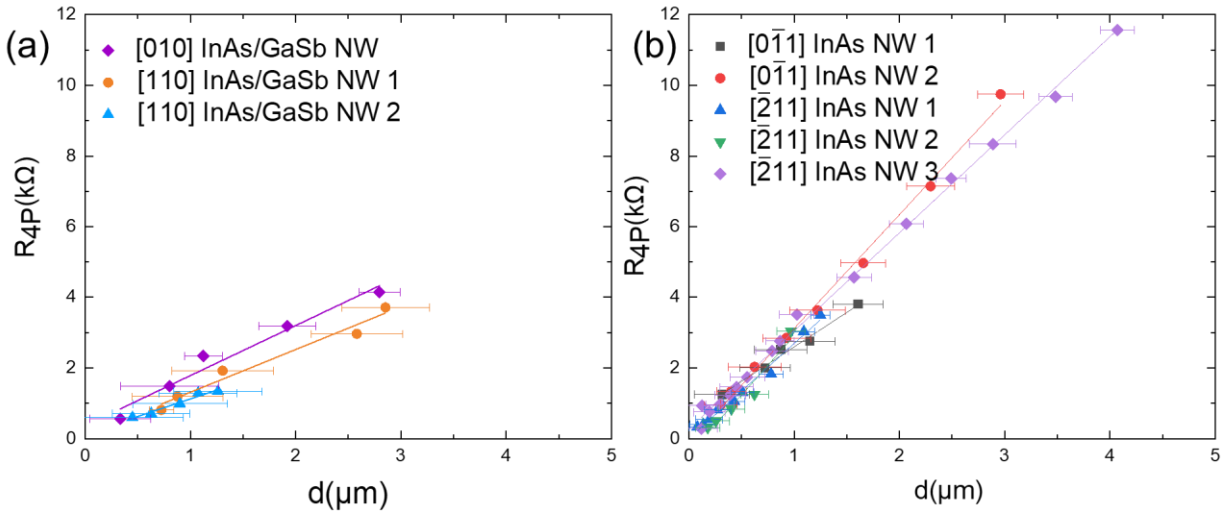

FIG. S7. Variation of the four-point probe resistance measured at different inner probe distances d on different 100 nm-wide (a) InAs/GaSb NWs of sample D and (b) InAs NWs of sample C. Lines are best linear fits of the point data.

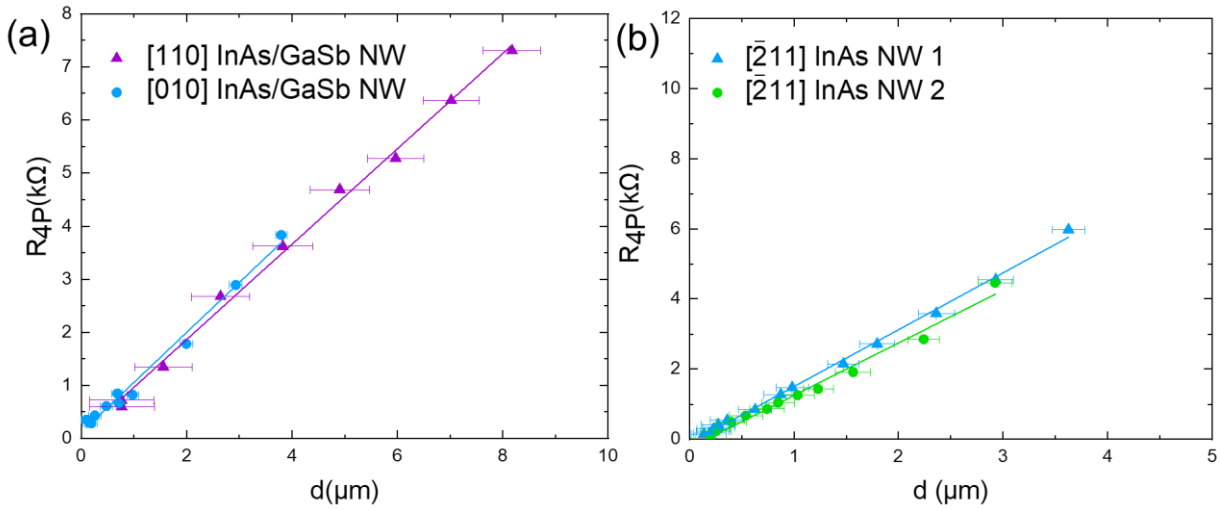

FIG. S8. Variation of the four-point probe resistance measured at different inner probe distances d on different 200 nm-wide (a) InAs/GaSb NWs of sample D and (b) InAs NWs of sample C. Lines are best linear fits of the point data.

REFERENCES

[1] www.nextnano.de/nextnano3/